Protective Iron Carbonate Films—Part 1: Mechanical Removal in Single-Phase Aqueous Flow

V. Ruzic,‡, M. Veidt,* and S. Nešić***

ABSTRACT

The protective role of iron carbonate films deposited on steel surfaces as by-products of carbon dioxide (CO_2) corrosion may be hindered by mechanical film removal due to hydrodynamic forces. Damage to the film is frequently accompanied by severe corrosive attack, which may ultimately result in costly equipment failure. The present work reports on experimental investigations of mechanical film removal (its kinetics and level of damage to the film) using a rotating cylinder configuration in the highly turbulent flow regime. Corrosion rate monitoring using the linear polarization resistance technique was used as a tool for implicit film removal rate measuring, whereas scanning electron microscopy served for verification and evaluation purposes. Two types of films were studied, one less uniform and adherent and the other more compact and adherent. The results clearly show that pure mechanical removal in undisturbed single-phase flow does occur. However, film removal starts after an initiation period and is only localized. The differences in the thickness, microstructure, and topography of intact and residual films are discussed in detail for both film types. In addition, the possible mechanism of mechanical film removal from the fluid mechanics point of view has been proposed.

KEY WORDS: carbon dioxide corrosion, erosion-corrosion, mechanical film removal, protective iron carbonate film, rotating cylinder electrode, single-phase flow, turbulent Taylor-Couette flow

Submitted for publication March 2005; in revised form, October 2005.

‡ Corresponding author. E-mail: v.ruzic@uq.edu.au.

* Department of Mechanical Engineering, The University of Queensland, Brisbane Queensland 4072, Australia.

** Institute for Corrosion and Multiphase Flow Technology, Chemical Engineering Department, Ohio University, 340 1/2 W. State St., Stocker Center, Athens, OH 45701.

INTRODUCTION

Mild steel is an inexpensive pipeline construction material frequently used in the oil and gas production and transportation industry; however, it is not inherently resistant to internal corrosion in the presence of carbon dioxide (CO_2), hydrogen sulfide (H_2S), organic acids, etc. It may be used safely in some cases when protective corrosion films form such as iron carbonate ($FeCO_3$). $FeCO_3$ is a by-product of CO_2 corrosion and may be deposited on the parent material. It slows down further corrosion by presenting a physical barrier that retards diffusion of corrosive species and by blocking the steel surface.[1] Therefore, any damage to this film is typically followed by a severe corrosive attack and may ultimately lead to costly equipment failure.[2]

Even though the exact mechanism of the film removal is still not well understood, the removal phenomenon in single-phase aqueous flow is commonly attributed to one or a combination of the two mechanisms:

—mechanical film removal by hydrodynamic forces,[3-6] and/or

—chemical film dissolution, which is believed to be governed by mass transfer.[7-9]

There are numerous studies of the hydrodynamics of turbulent flows and the impact on mechanical film removal. In some initial work, a commonly used parameter used as a criterion for the onset of mechanical removal was the critical or breakaway velocity.[10-12] However, this concept lacked universality and could not be used in different flow geometries.[13] Efird introduced the critical wall shear stress as the

0010-9312/06/000079/$5.00+$0.50/0

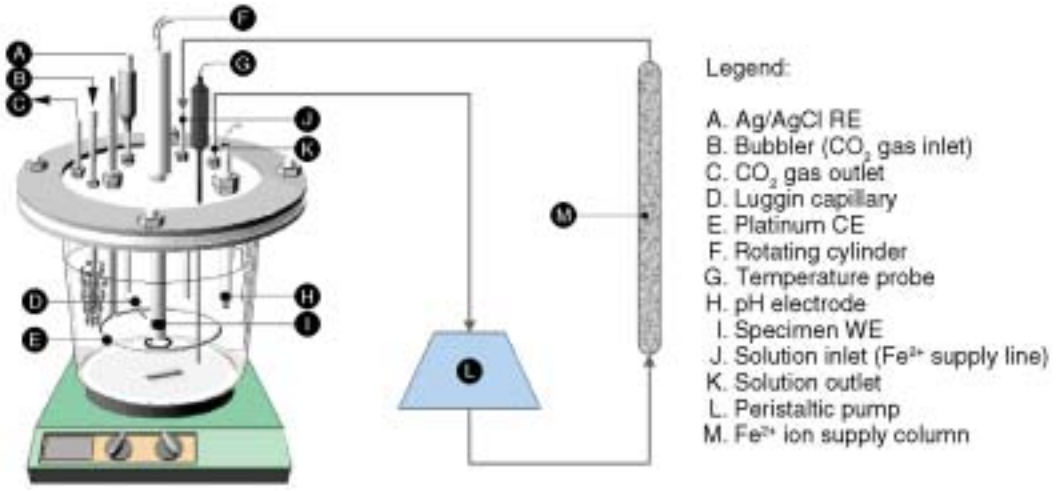

FIGURE 1. *Schematic shows the glass cell setup.*

defining factor for mechanical film degradation.[14] Silverman[15] related wall shear stress to mass transfer, rendering Efird's[14] approach applicable to film dissolution as well. Syrett[16] and Schmitt, et al.,[17] have argued that critical shear stress values are too small to be responsible for mechanical film disruption. The near-wall turbulence intensities also were often quoted to play a decisive role.[4-5,18-19] Based on flow simulations, Nešić and Postlethwaite showed that in disturbed flow geometries the mean wall shear stress was zero, close to the point of flow reattachment, where maximum metal loss was observed, while the local level of near-wall turbulence was at its highest level.[4-5] Their results questioned the once widely accepted proposal by Efird[14] on the applicability of mean wall shear stress. The most recent findings for a rotating stepped cylinder suggest that the fluctuating wall shear stress correlates much better with mass transfer than the mean wall shear stress.[19] The authors concluded that the former might be the "missing link," i.e., the determining factor for erosion-corrosion. Schmitt, et al., propose that intrinsic stresses rather than hydrodynamic forces could cause film cracking.[17] According to them, the intrinsic stresses originate from the volume mismatch between the metal surface and the growing $FeCO_3$ scale.

The present work reports on experimental investigations of mechanical film removal in undisturbed single-phase turbulent flow.

EXPERIMENTAL PROCEDURES

Corrosion experiments were conducted utilizing a three-electrode electrochemical system in a glass cell. A cylindrical specimen outer diameter (OD) by height (H) (12 mm by 10 mm) manufactured from 1020 mild steel with a ferritic-pearlitic microstructure was mounted onto a rotating shaft and served as a working electrode (WE). A 0.7-mm annular platinum wire and a saturated silver/silver-chloride (Ag/AgCl) electrode served as a counter (CE) and reference electrode (RE), respectively (Figure 1). More detailed information on glass cell setup and film growth procedures were published previously by Ruzic and Nešić.[20] The system operated at 80°C with an atmospheric pressure of 101 kPa. The partial pressure of the CO_2 gaseous phase was 0.54 bar at 80°C. A potentiostat was used for electrochemical corrosion measurements, whereas scanning electron microscopy (SEM) was used to characterize film morphology, thickness, and surface topography. Elemental compositional analysis of the corrosion products was also done by using the quantitative energy-dispersive spectroscopy (EDS).

Film Formation

$FeCO_3$ films were grown in-situ by precipitation in a chemically controlled aqueous environment. The electrolyte was prepared by adding 1 wt% sodium chloride (NaCl) to distilled water, which was then deaerated by sparging CO_2 gas for at least 30 min and then heated up to 80°C. To stimulate film growth by reaching high supersaturation with respect to iron carbonate, a "source" of ferrous ions (Fe^{2+}) was provided by using fine mild steel wool packed in a separate glass column connected via flexible tubing to the main cell (Figure 1). The electrolyte was continuously recirculated through the column by means of a peristaltic pump at 0.5 L/min flow rate, adding Fe^{2+} to the main glass cell. The Fe^{2+} bulk concentration was measured using the phenanthroline calorimetric method. The desired pH value (pH 6.9) was adjusted by adding sodium hydrogen carbonate ($NaHCO_3$) as required. Prior to immersion the steel specimen was ground with 1000-grit silicon carbide (SiC) paper, degreased with acetone (CH_3COCH_3), rinsed with ethanol (C_2H_5OH) and dried.

$FeCO_3$ films were grown at "mild" hydrodynamic conditions, 200 rpm rotational speed (peripheral

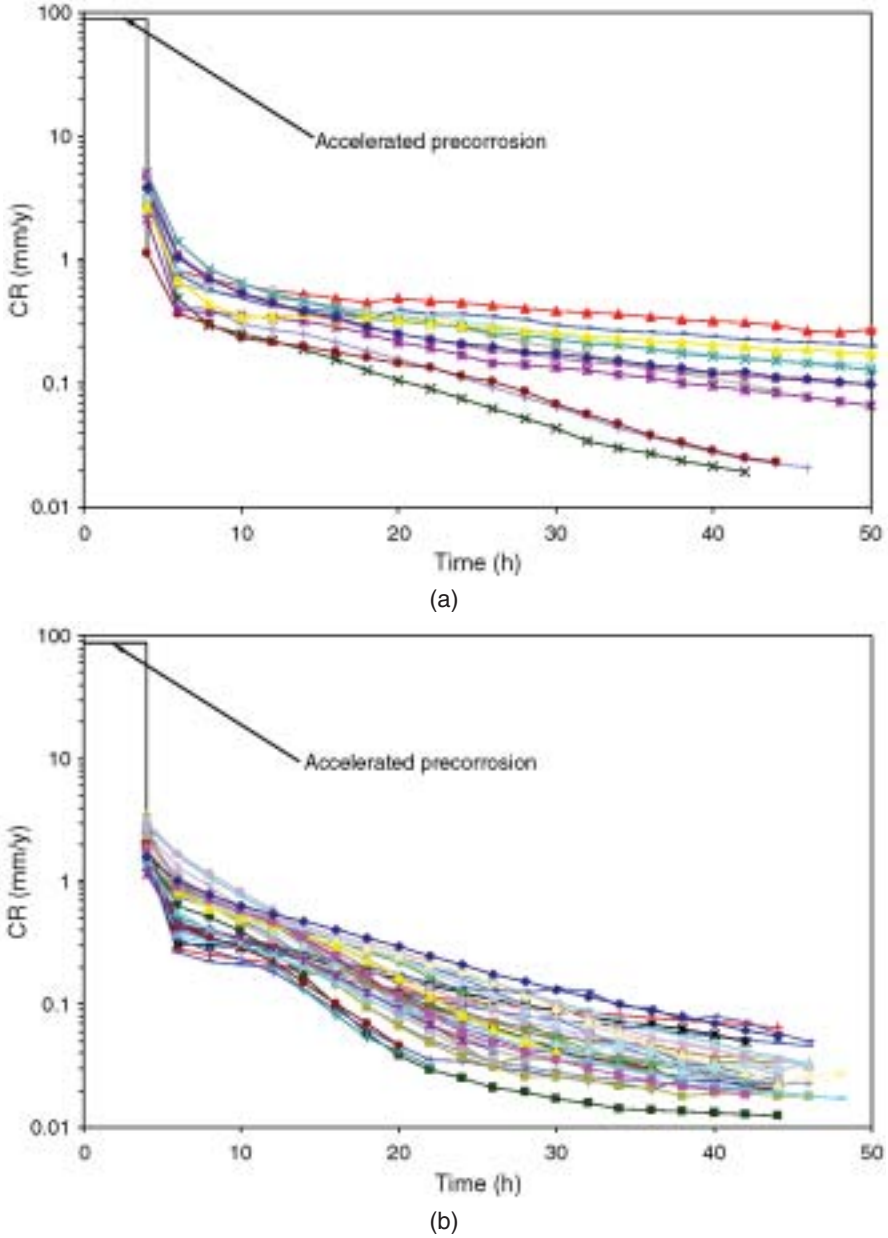

FIGURE 2. *Corrosion rate reduction during: (a) type A and (b) type B film formation following 4 h of accelerated precorrosion at 10 µm/h rate.*

velocity, v = 0.13 m/s; Reynolds number, Re = 3.68 × 10^3). At the very beginning of film formation, the steel specimen (WE) was subjected to "forced precorrosion" by passing a 28.39-mA anodic current (corresponding to 10 µm/h forced metal dissolution) over a 4-h period. Subsequently, it was allowed to corrode spontaneously for up to two days, which proved to lead to much thicker and more reproducible films than in spontaneous corrosion alone.[20] There were two types of film considered for further study: type A and type B films. Both were grown using the previously described procedure, except that for type A films the pH adjustment was made prior to accelerated pre-corrosion, whereas for type B films, the sequence was reversed.

The film growth was followed indirectly by measuring the corrosion rate (CR) using the linear polarization resistance (LPR) technique. The specimen was polarized every 2 h from –20 mV to 20 mV with respect to open-circuit potential by using a scan rate of 0.125 mV/s.

Mechanical Film Removal

Once a very protective film had been formed (which was judged when the CR ≤ 0.05 mm/y), the external Fe^{2+} supply to the cell was stopped. The solution was kept at a very slightly supersaturated level to eliminate further precipitation, but also to prevent film dissolution. This supersaturation was checked

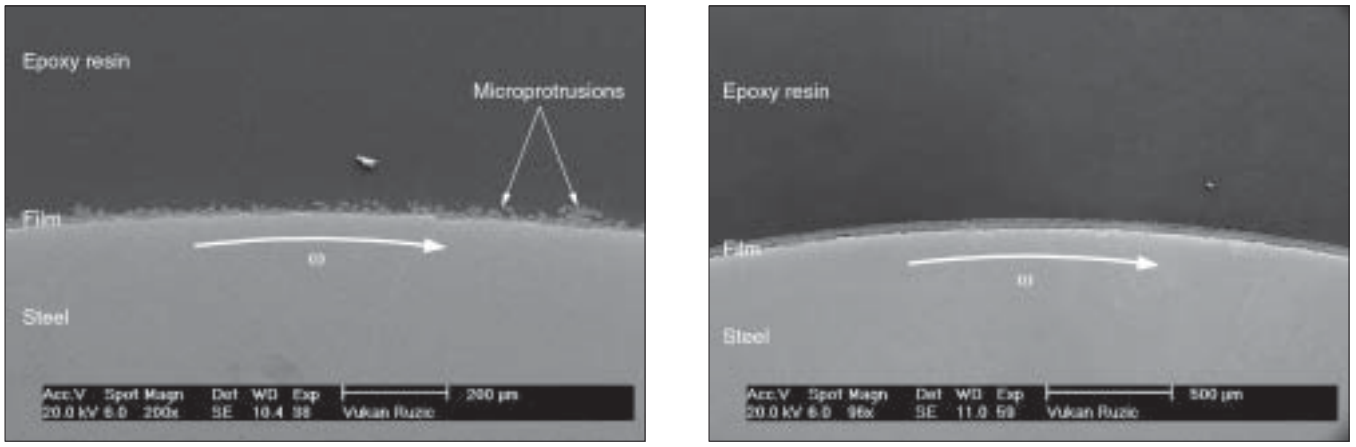

(a) (b)

FIGURE 3. *Typical cross section of: (a) type A (mag. 200X) and (b) type B (mag. 100X) $FeCO_3$ film at the end of formation process.*

regularly by measuring the pH and the Fe^{2+} bulk concentration. The gas sparger was withdrawn into the gas phase to minimize any flow disturbance.

To achieve mechanical film removal, the rotational speed was increased. Two rotational speeds, 7,000 rpm (v = 4.40 m/s; Re = 1.29×10^5) and 10,000 rpm (v = 6.28 m/s; Re = 1.84×10^5) were used. The removal process was followed implicitly using LPR and then verified using SEM and EDS. During the mechanical removal phase, LPR scans were repeated every 10 min by scanning at a faster rate compared to film formation (0.5 mV/s). Once the CR stabilized, the specimens were removed, immediately rinsed with ethanol, dried, and cut into two parts—one to be mounted in epoxy resin for film cross-sectional examination and the other one for surface surveying. The former was cut using a diamond saw, ground with 600-, 800-, 1000-, and 1200-grit SiC paper, polished with 6-, 3-, 1-, and 1/4-μm diamond paste, and finally platinum-coated before loading into the SEM chamber.

RESULTS

Film Formation

Initial, film-free corrosion rate was measured to be CR = 1.5 ± 0.1 mm/y. Following the 4-h accelerated pre-corrosion period, corrosion rates decreased rapidly. There was a significant variation in the final corrosion rate for type A film, as shown in Figure 2(a). In some cases, very protective films were formed (CR < 0.05 mm/y) in less than 2 days, while in others the decline in the corrosion rate was much slower. This lack of repeatability for the type A film formation procedure was considered a problem that would affect subsequent film removal steps, and therefore an alternative, more repeatable procedure was sought.

Figure 2(b) shows the corrosion rate reduction curves for type B films. It can be noticed that generally the corrosion rate decline was more rapid, reaching values CR ≤ 0.05 mm/y within a day or two at most when compared to type A films. More importantly, the type B procedure yielded significantly less variability in the results. Although far smaller than in type A films (by a factor of 5.4), the spread in the final corrosion rate is still large, but one can argue that in all cases CR < 0.1 mm/y, which can be considered a protective situation.[21]

Figure 3 shows cross-sectional micrographs of type A and B films, while magnified details of typical cross-sectional areas are presented in Figure 4. Similarly, surface topography SEM images are shown in Figure 5 with magnified views given in Figure 6. For type A films the film thickness ranged from 15 μm to 25 μm, while type B films were approximately twice as thick (40 μm to 50 μm). Pits were seen beneath type A films as well as nonuniform protrusions. The protrusions manifested as a microscale surface roughness, i.e., microprotrusions (height range: 10 μm to 20 μm), and macroscale humps above pits, i.e., macroprotrusions (height range: couple of hundreds of microns to up to 1,000 μm). In contrast, the surface of type B films was smooth and no pits were observed. The observed lines on the film surface (Figure 5[b]) are named "flow marks," since they arise from a flow-assisted action during the precipitation process. The preferred alignment of grains, i.e., crystal growth, was in the circumferential flow direction.

Mechanical Film Removal

Following the increase of velocity, corrosion rates were accelerated due to protective film failure and removal. This did not happen immediately. Instead, there was an initiation period related probably to slow initiation and growth of cracks in the film. Corrosion rate rise curves for both film types are shown in Figure 7. The main mechanical film removal results are

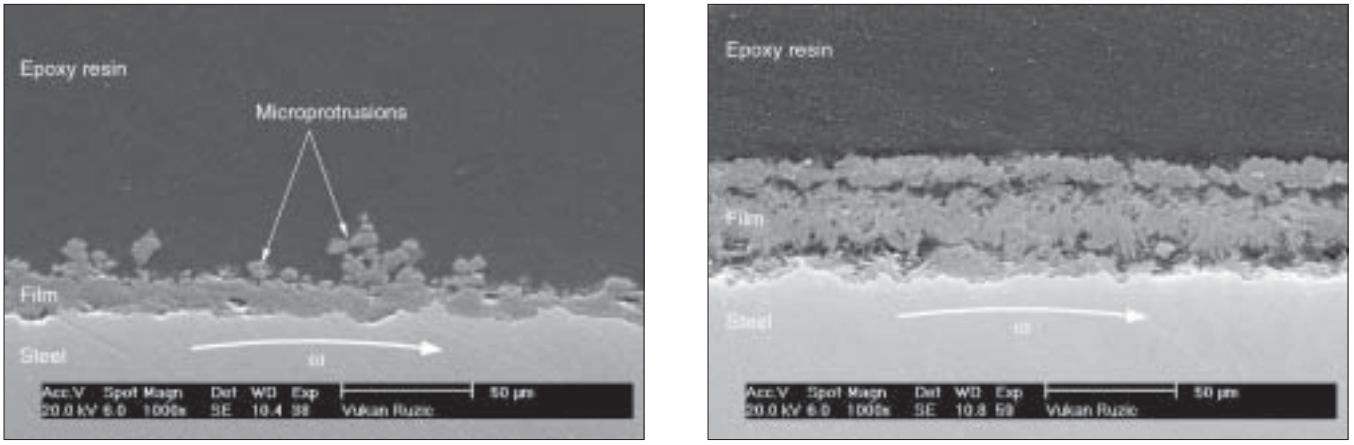

(a) (b)

FIGURE 4. *Typical cross section of: (a) type A and (b) type B $FeCO_3$ film at the end of formation process (mag. 1,000X).*

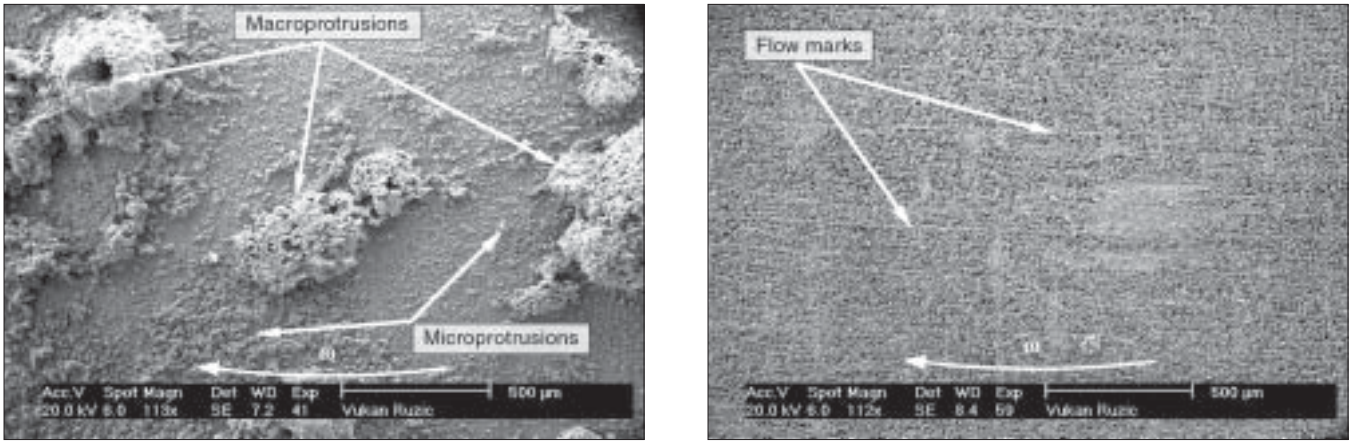

(a) (b)

FIGURE 5. *Typical surface topography of: (a) type A and (b) type B $FeCO_3$ film at the end of formation process (mag. 100X).*

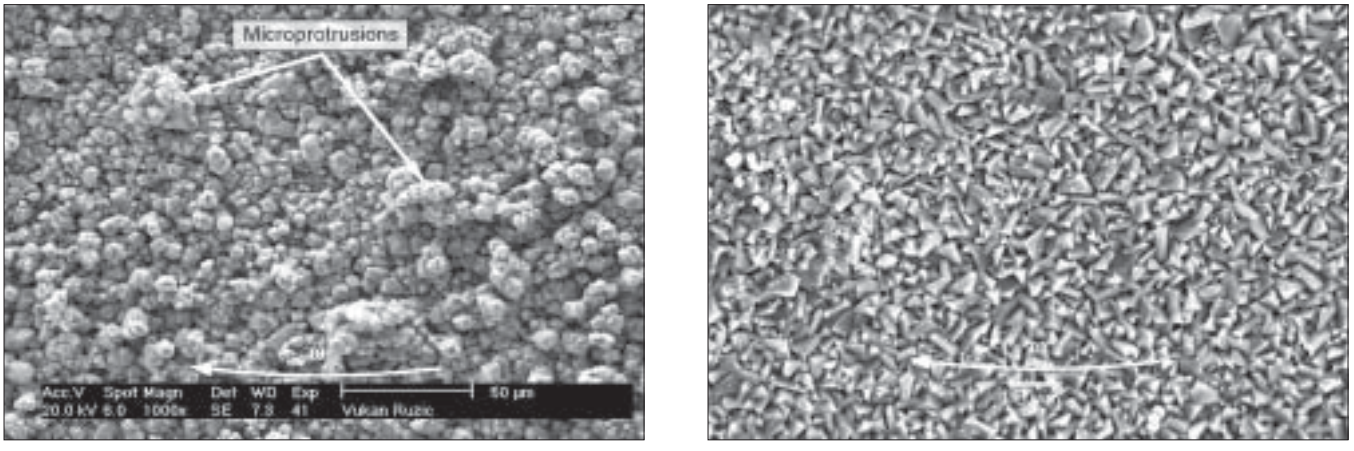

(a) (b)

FIGURE 6. *Typical surface topography of: (a) type A and (b) type B $FeCO_3$ film at the end of formation process (mag. 1,000X).*

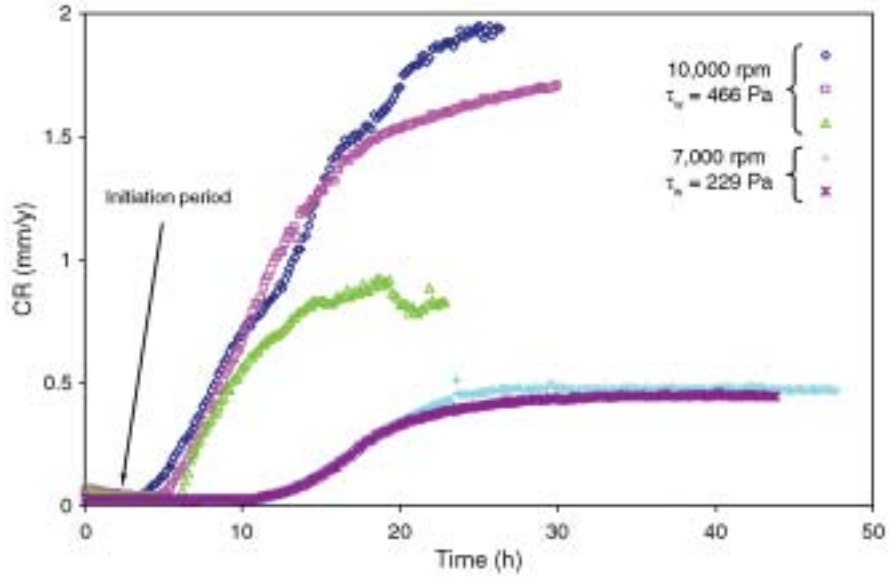

(a)

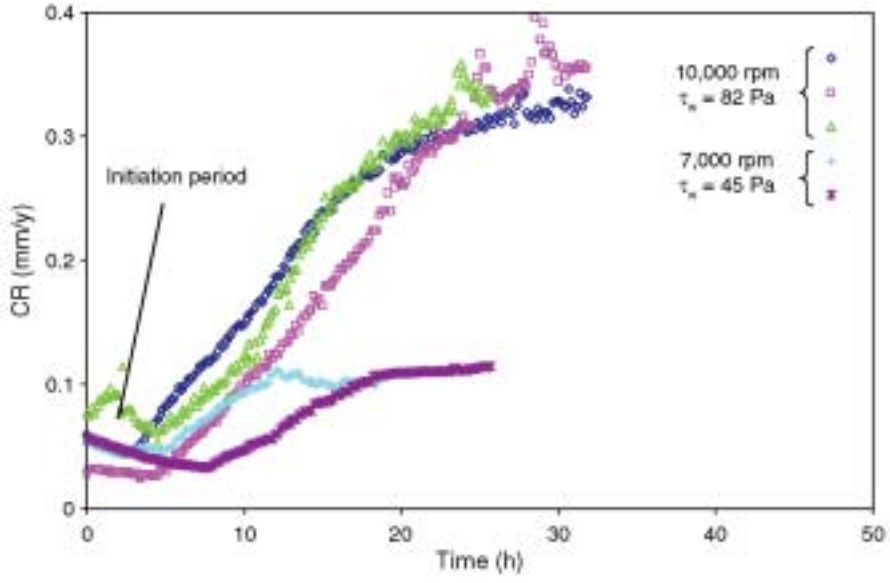

(b)

FIGURE 7. *Corrosion rate increase during mechanical removal of: (a) type A and (b) type B films at 10,000 rpm and 7,000 rpm rotational speed.*

summarized in Table 1. At a higher velocity the corrosion rates increased much faster, indicating a more effective film failure/removal process. All experiments were terminated at the point when the corrosion rates showed a tendency to stabilize. Some experiments at 7,000 rpm were kept conducted for a prolonged period of time after corrosion rates had reached a plateau, to check whether a delayed "second wave" of film removal was going to occur. However, this was not observed even when the exposure time was doubled. A good reproducibility with respect to the slope of the corrosion rate increase, as well as the mean final corrosion rate, was obtained in most experiments. Generally, films of type A exhibited much higher mean final corrosion rates than type B films, indicating a lower level of protection by the surviving film. The "kinks" periodically seen on the corrosion rate curves can be explained by transient flow disturbances that stem from submerging measuring equipment (pH electrodes, probes, syringes, etc.) into the solution, which was necessary for process control.

The SEM inspection of samples confirmed that film removal was partial. Figure 8 shows a top-view appearance of the damaged type A film surface at low and high velocity. The number of damaged film locations was significantly smaller at the lower velocity, which is in agreement with the measured corrosion rates (Figure 7). The size of the damaged film areas

TABLE 1
Summary of Main Mechanical Film Removal Results[A]

Mechanical Removal Experiments	Rotational Speed (rpm)	Mean Final CR (mm/y)	Mean CR Gradient (mm/y/h)	Mean Removal Time (h)	Mean Initiation Time (h)
Type A films	7,000	0.46 ± 0.01	0.0402 ± 0.0019	9.0 ± 2.0	11.0 ± 0.3
	10,000	1.49 ± 0.34	0.1147 ± 0.0053	10.7 ± 2.4	4.9 ± 0.8
Type B films	7,000	0.11 ± 0.01	0.0078 ± 0.0008	8.9 ± 1.9	6.5 ± 1.3
	10,000	0.34 ± 0.01	0.0162 ± 0.0007	15.3 ± 1.0	4.2 ± 0.5

[A] Experimental uncertainties represent standard deviation of the mean, i.e., standard error.

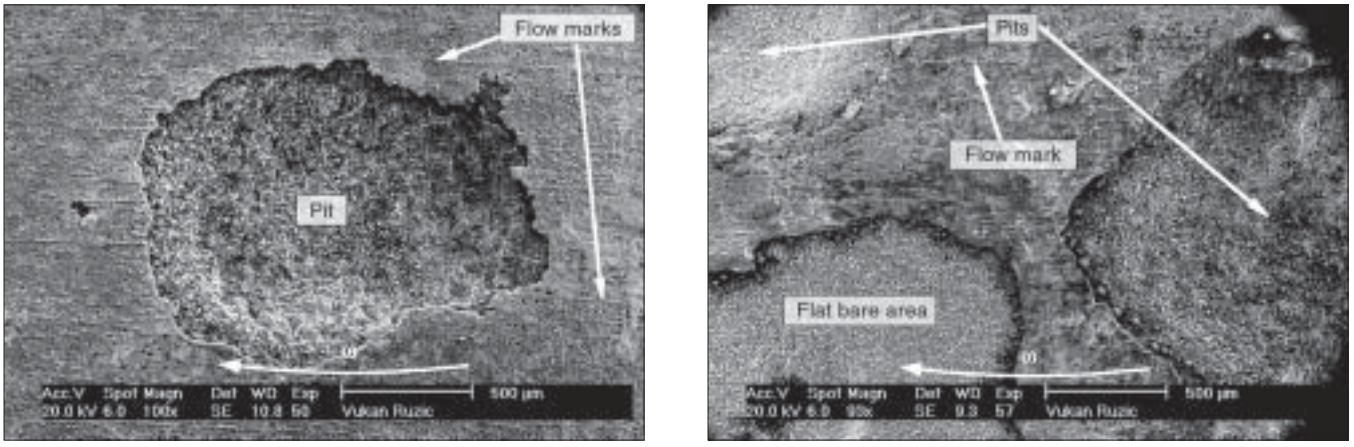

(a) (b)

FIGURE 8. *Typical surface topography of type A postremoval $FeCO_3$ film at: (a) 7,000 rpm and (b) 10,000 rpm (mag. 100X).*

varied from a couple of hundreds of microns to a couple of millimeters. The majority of the film failure areas coincided with underlying pits, as shown in the cross-sectional images of the type A films in Figure 9. Cross-sectional images of the "undamaged" type A film featured long circumferential cracks very close to the metal surface, as shown in Figure 10, indicating a rather poor adhesive strength of these films.

At a lower film removal velocity, much of the type B film appeared to have survived the mechanical film removal process with only a few isolated damaged patches (Figure 11). However, at a higher velocity a large number of film damage locations was seen (Figures 12 and 13[b]). The unique characteristic of type B films was the presence of superficial cracks, as shown in Figures 11 and 13(a), which were more prevalent at the lower velocity. This seems to suggest that the process of cracking at a lower velocity did not progress to the stage of film removal, which would produce visibly damaged areas as seen at a higher velocity. It is interesting to note that the crack orientation was always vertical, i.e., parallel to the specimen axis of rotation and perpendicular to the flow direction. This phenomenon can be explained considering residual stresses created during film formation at a low velocity (200 rpm). The flow marks discussed above indicate the preferred crystal growth in the circumferential direction (Figures 5[b] and 8). It seems that because of the small but finite circumferential shear stresses the cohesion strength in this direction is slightly smaller than in the axial direction. In consequence, crack orientation occurs perpendicular to the weak direction, i.e., in the axial direction as observed. Overall, the results suggest better mechanical properties of the type B film compared to the type A film, which was borne out by the corrosion rate measurements (Figure 7). The adhesive strength of type B films appeared to be better as well, as indicated by the absence of circumferential cracks in the cross-sectional images of residual type B films shown in Figure 14.

It is important to note that exposure to mechanical film removal did not cause a decrease in the global film thickness by means of hydrodynamic shearing, which can be easily confirmed by comparing film thicknesses before (Figure 4) and after the mechanical removal phase (Figures 10 and 14).

To get further insight into the nature of film damage, portions of the film that survived the experiments (encircled region in Figure 12) were magnified 2,000 times and shown in Figure 15. Portions of the film were also subjected to EDS, capable of chemical analysis of constituent elements by monitoring sec-

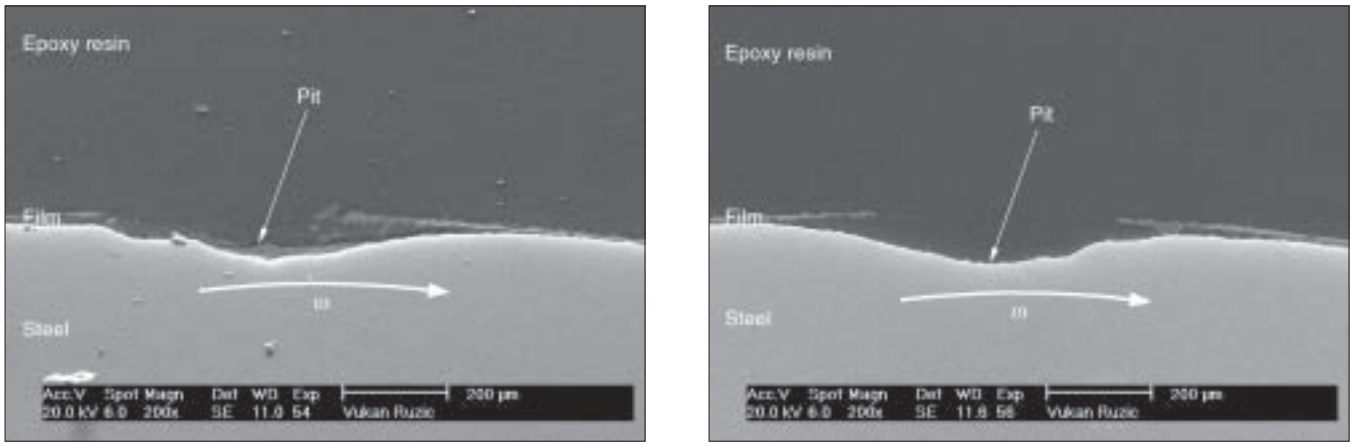

(a) (b)

FIGURE 9. *Cross section of type A postremoval $FeCO_3$ film showing bare pit at: (a) 7,000 rpm and (b) 10,000 rpm (mag. 200X).*

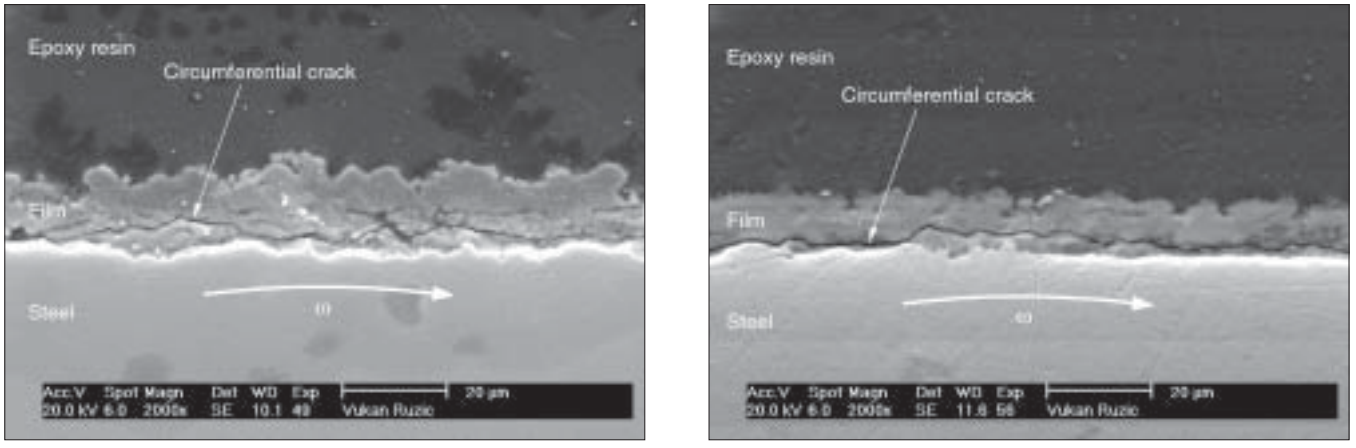

(a) (b)

FIGURE 10. *Typical cross section of preserved type A postremoval $FeCO_3$ film featuring detachment at: (a) 7,000 rpm and (b) 10,000 rpm (mag. 2,000X).*

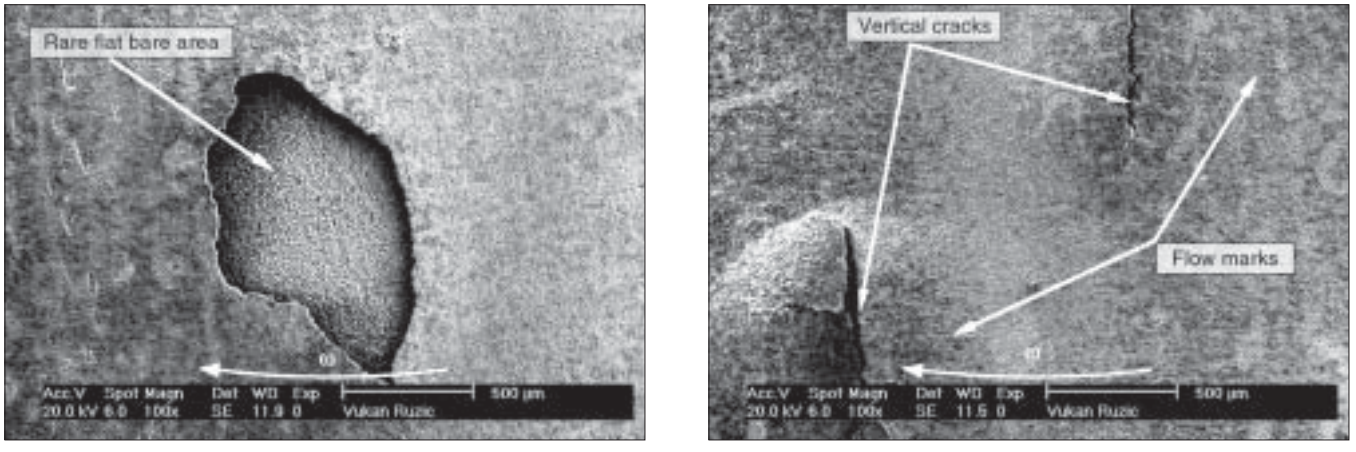

(a) (b)

FIGURE 11. *Typical surface topography of type B postremoval $FeCO_3$ film at 7,000 rpm featuring: (a) few film-free areas and (b) lots of vertical cracks (mag. 100X).*

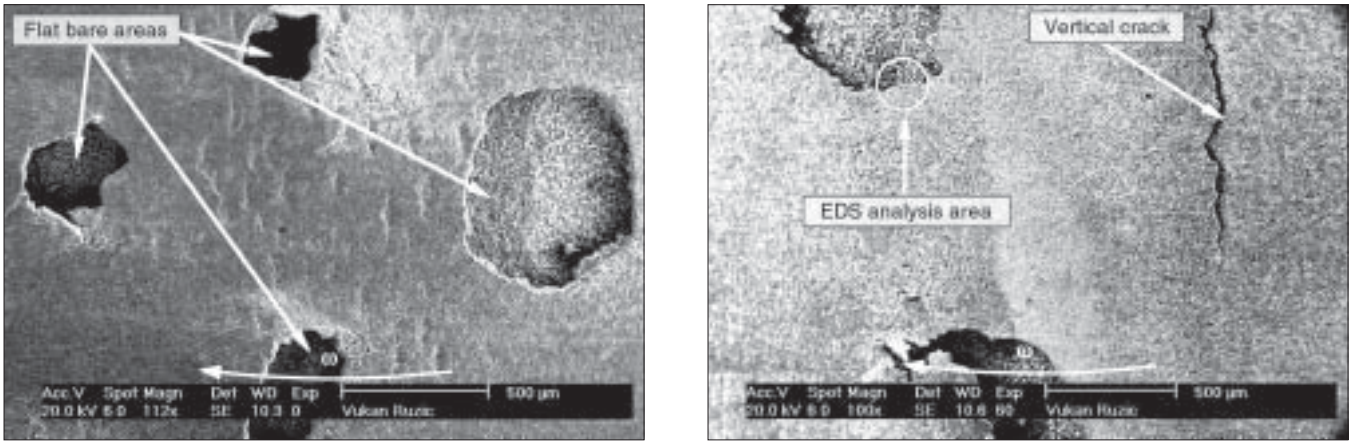

(a) (b)

FIGURE 12. *Typical surface topography of type B postremoval $FeCO_3$ film at 10,000 rpm featuring: (a) lots of film-free areas and (b) few vertical cracks—encircled region denotes magnified area of interest (Figure 15) on which EDS analysis was performed (mag. 100X).*

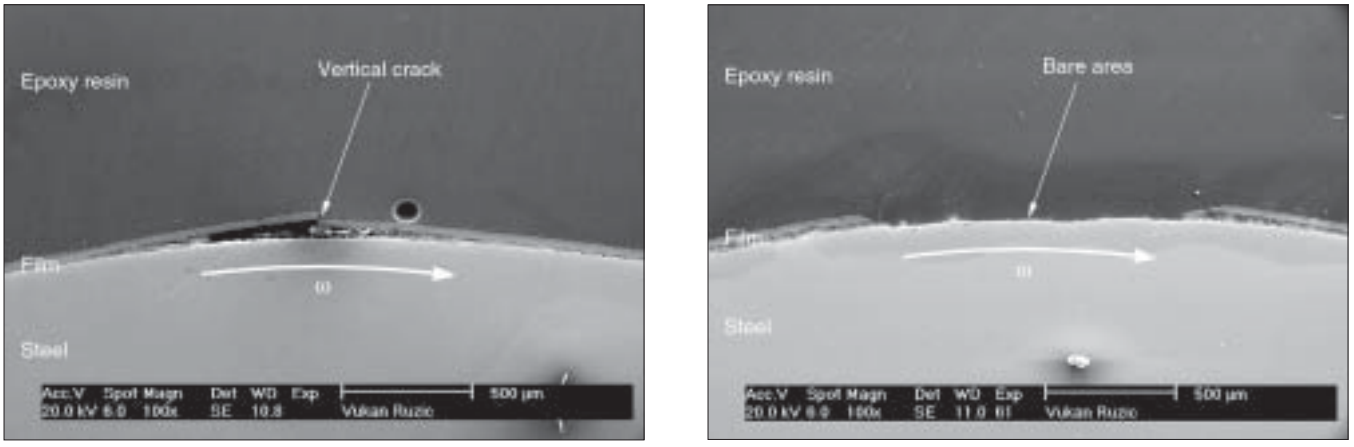

(a) (b)

FIGURE 13. *Cross section of type B postremoval $FeCO_3$ film featuring typical damage: (a) crack with lifted-off film edge at 7,000 rpm and (b) pit-free bare area at 10,000 rpm (mag. 100X).*

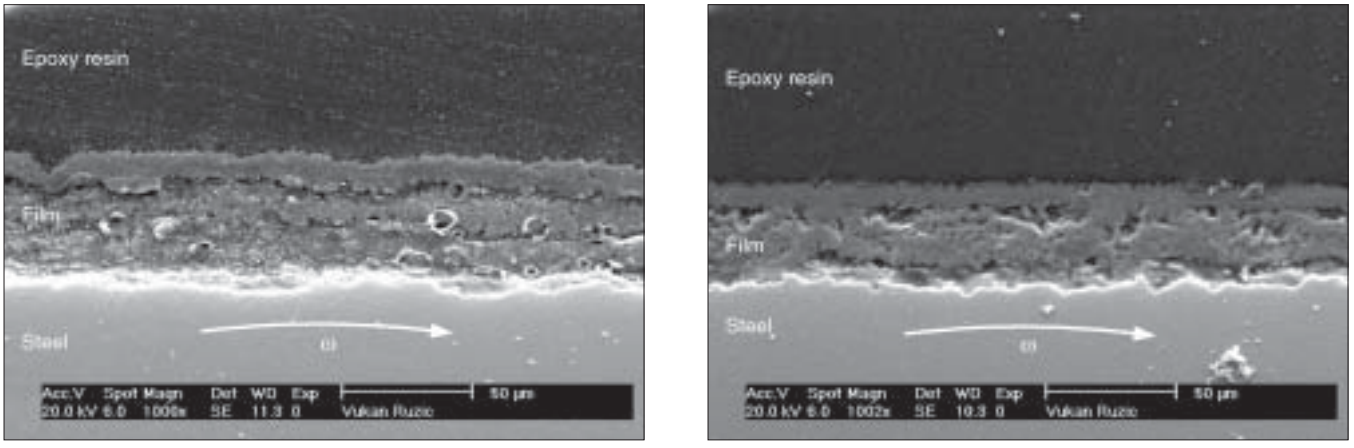

(a) (b)

FIGURE 14. *Typical cross section of preserved type B postremoval $FeCO_3$ film featuring intact, well-adhered layer at: (a) 7,000 rpm and (b) 10,000 rpm (mag. 1,000X).*

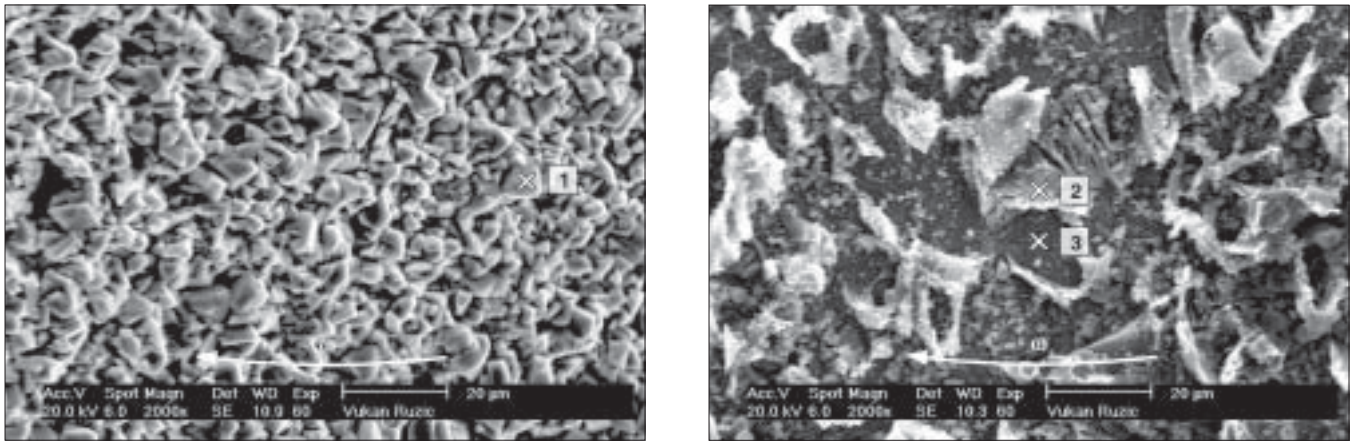

(a) (b)

FIGURE 15. *Typical surface topography of type B postremoval $FeCO_3$ film at 10,000 rpm showing: (a) preserved and (b) film-free area (mag. 2,000X).*

ondary x-rays. Produced spectra are given in Figure 16, while the quantified elemental data showing weight and atomic percentages of iron, carbon, and oxygen content are presented in Table 2. Elemental analysis confirmed that the tightly packed crystal grains seen in the undamaged film were pure $FeCO_3$, since the Fe:C:O atomic ratio was an ideal 1:1:3 proportion (Table 2, location 1). Conversely, the damaged film region revealed two distinct phases: flat, dark gray regions with scattered whitish flakes (sized 10 μm to 20 μm), as seen Figure 15. The flakes were also identified as pure $FeCO_3$, i.e., remnants of the protective film. Although the C:O ratio nicely obeyed the 1:3 requirement, there was a 10% surplus in the iron content (Table 2, location 2), which was also indicated by higher Fe peaks shown in the EDS spectrum compared to the preserved $FeCO_3$ layer spectrum (Figure 16). The minor presence of the Fe phase along with $FeCO_3$ is most likely due to the fact that the flake thickness was slightly smaller than the examined volume, which typically was 5 μm to 6 μm in diameter. In consequence, a small portion of the substrate beneath the flake was picked up by the detector. As expected, the dark flat areas represented the bare metal, since EDS confirmed Fe to be the only detected element (Figure 16 and Table 2, location 3).

DISCUSSION

Flow Hydrodynamics

According to Gabe, et al.,[22] the critical Reynolds number for transition from laminar to turbulent flow for a rotating cylinder (RC) geometry is Re = 200 (where $Re = vd/\nu$, $v = \omega d/2$ is the peripheral velocity in m/s, ω is the angular speed in rad/s, d is the diameter of the cylindrical specimen in m, and ν is the kinematic viscosity of the solution in m^2/s). The kinematic viscosity of the solution was calculated to be $\nu = 0.41 \times 10^{-6}$ m^2/s at 80°C (following Schmitt and Mueller[23]). It appears that for current conditions the turbulent flow was achieved already for rotational velocity as low as 11 rpm (v = 0.007 m/s). Therefore, all the experiments discussed above, i.e., mechanical film removal at 7,000 rpm (v = 4.40 m/s; $Re = 1.29 \times 10^5$) and 10,000 rpm (v = 6.28 m/s; $Re = 1.84 \times 10^5$), were conducted in very turbulent flow.

The wall shear stress at the film surface may be determined from the friction loss along the surface circumferential line by:

$$\tau_w = \left(\frac{f}{2}\right)\rho v^2 \qquad (1)$$

where τ_w is the drag shear stress at the wall in Pa, f is the Fanning friction factor, and ρ is the solution density in kg/m^3. The density of the solution (ρ = 1,000 kg/m^3) at 80°C was obtained from the literature.[23]

The friction factor for smooth cylinders can be calculated using the Theodorsen-Regier empirical friction law:[24]

$$\log Re = 0.1737\left(\frac{f}{2}\right)^{-\frac{1}{2}} - \log\left(\frac{f}{2}\right)^{\frac{1}{2}} + 0.2979 \qquad (2)$$

Eisenberg, et al., simplified the above correlation for smooth rotating cylinders in the turbulent flow regime and approximated it to:[25]

$$\frac{f}{2} = 0.0791\,Re^{-0.3} \qquad (3)$$

It is also well documented that, for rough surfaces, the drag on the rotating cylinder becomes dependent on roughness dimension (ε) rather than Re. The proposed modified Theodorsen-Regier equation, which

was found to be valid for roughnesses produced by corrosion, is given as:[26]

$$\left(\frac{f}{2}\right)^{-\frac{1}{2}} = 1.25 + 5.76\log\left(\frac{d}{\varepsilon}\right) \quad (4)$$

Kappesser, et al., presented an approximate relation that determines the "critical value" of the Reynolds number at which the friction factor ceases to be dependent on angular velocity, but rather becomes related to surface roughness:[27]

$$Re_{crit} = \left(11.8\frac{d}{\varepsilon}\right)^{1.18} \quad (5)$$

The shear stress is compared for two film types in Figure 17. For the purpose of shear stress calculation, the average grain size for type B films before mechanical film removal was estimated to be 5 μm to 7 μm from Figure 6(b). The characteristic roughness dimension was assumed to be half of that size (ε ≈ 3 μm), considering that at least a half of each grain was embedded in the film. Since the Reynolds number for higher velocity (Re = 1.84×10^5) was smaller than the critical value ($Re_{crit} = 3.28 \times 10^5$) calculated using Equation (5), type B films were considered to be smooth. Hence, the Eisenberg correlation for smooth surfaces given by Equation (3) was applied. In contrast, the average macroprotrusion height was assumed to be the characteristic roughness dimension in the case of type A films. The average value was determined as a half of the maximum macroprotrusion height, i.e., ε ≈ 500 μm. Therefore, since the computed value of Re_{crit} = 782 was much smaller than the actual Re for 10,000 rpm rotational speed, type A films were judged as rough surface cylinders with a relative roughness (ε/d) of 4.2×10^{-2}. Accordingly, empirical correlation as in Equation (4) was related to this type of film. For two rotational speeds of interest (7,000 rpm and 10,000 rpm), predicted wall shear stress values were 45 Pa and 82 Pa for type B (smooth) film vs. 229 Pa and 466 Pa for type A (rough) film. It can be concluded that shear stress roughly doubled at high velocity when compared to low velocity. It also increased by a factor of 5.1 to 5.7 for rough surface films in comparison to smooth surface films. It has been shown previously that the maximum magnitude of the instantaneous wall shear stress fluctuations can be three to four times larger than the maximum mean value.[19] However, such wall shear stresses occur locally and intermittently in the flow-disturbed region; therefore, it is not likely that this factor would be applicable to an undisturbed situation that is present here. Either way, it seems that the wall shear stress values (both mean and fluctuating) are too small to be the only determining factor for the mechanical removal of $FeCO_3$ films in single-phase flows.

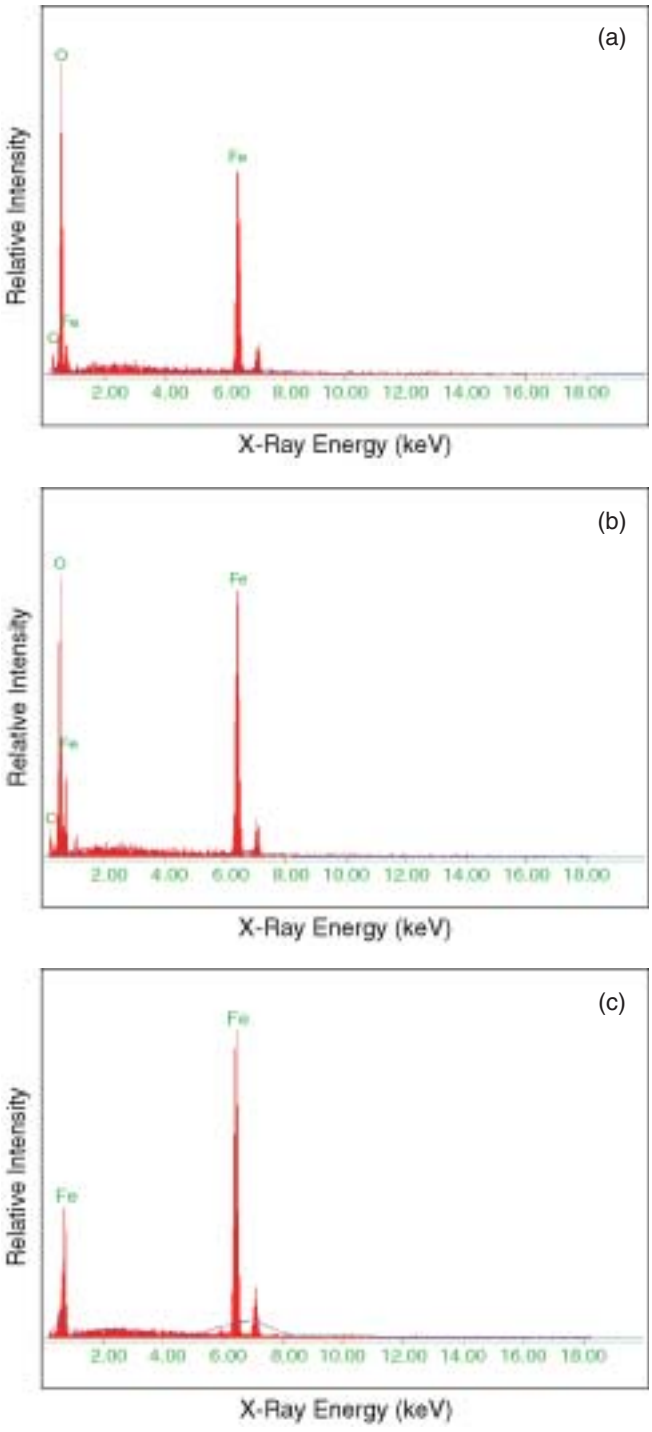

FIGURE 16. *EDS spectra of: (a) preserved film layer (location 1), (b) film-free area—flake (location 2), and (c) film-free area—substrate (location 3), after type B mechanical removal at 10,000 rpm. The examined locations are designated in Figure 15.*

At least, from the fracture mechanics standpoint, it would be expected that a completely different character of the damage would have been observed if the shear forces had been solely responsible. Namely, one would hope to see circumferentially elongated types of film-free areas as a result of a shearing action rather

TABLE 2
Chemical Composition of Preserved Film Layer (Location 1) and Film-Free Area (Locations 2 and 3) After Type B Mechanical Removal at 10,000 rpm Rotational Speed

Sample	Location 1 (Preserved Film—Grain)			Location 2 (Film-Free Area—Flake)			Location 3 (Film-Free-Area—Substrate)		
Element	Fe	C	O	Fe	C	O	Fe	C	O
wt%	46.88	10.69	42.43	58.35	8.22	33.43	100	—	—
at%	19.16	20.31	60.53	27.36	17.92	54.72	100	—	—

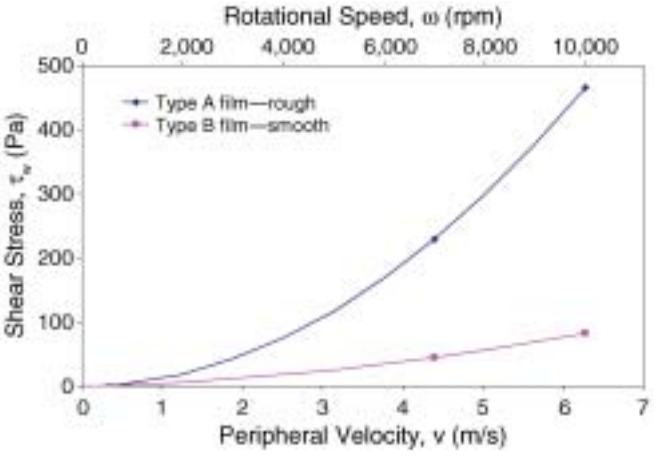

FIGURE 17. *Calculated shear stress vs. peripheral velocity (rotational speed) at T = 80°C for (—◆—) rough type A and (—■—) smooth type B films.*

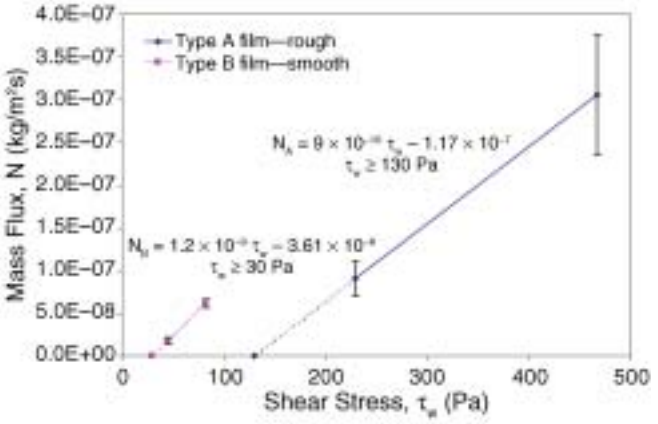

FIGURE 18. *Variation of the average mass flux of Fe^{2+} species due to accelerated corrosion caused by film loss with calculated mean wall shear stress at T = 80°C for type A (rough) and type B (smooth) films (bars represent propagated standard error).*

than mostly vertically oriented ones (Figures 11 and 12). In support of this hypothesis is the fact that $FeCO_3$ adherence strengths (ranging from 1 MPa to 30 MPa) and estimated critical fracture stresses (ranging from 10^2 MPa to 10^3 MPa) are many orders of magnitude larger than the wall shear stress exerted by the fluid at the film surface.[17] Therefore, other hydrodynamic parameters have to be considered as well.

Notwithstanding the judgment that mean wall shear stress is not likely the only factor accountable for mechanical film removal, its "critical value" might still serve the purpose to provide a reference point at which the film disruption occurs. Giralt and Trass demonstrated that erosion rates expressed via mass flux increased linearly with wall shear stress in situations when they played an important, although not necessarily exclusive, role during the mechanical removal mechanism.[8] In this study the film removal rates could not be obtained directly by using the weight-loss technique because of the in-situ nature of the experiments; hence, the flux of Fe^{2+} ions from the metal surface due to the corrosion process, which is indirectly related to film removal, was used for this purpose. Therefore, the mass flux of Fe^{2+} at the wall N (kg/m^2s) was obtained from the rate of corrosion rate increase as:

$$N = \rho_s CR_{grad} \Delta t \quad (6)$$

where ρ_s = 7,874 kg/m^3 and is the steel density, CR_{grad} is the corrosion rate slope (m/s^2), i.e., change in the magnitude of film removal, and Δt is the time interval during which mechanical film removal takes place (s), i.e., the period between the onset and slow down of mechanical film removal (Table 1). The variation of the average mass flux with calculated mean wall shear stress for both film types is shown in Figure 18, assuming the linear relationship between N and τ_w. The regression lines for mechanical film removal conditions fitted through low- and high-velocity data points for type A and B films are given by:

$$N_A = 9\times10^{-10}\tau_w - 1.17\times10^{-7} \quad \text{for } \tau_{wA} \geq 130 \text{ Pa} \quad (7)$$

$$N_B = 1.2\times10^{-9}\tau_w - 3.61\times10^{-8} \quad \text{for } \tau_{wB} \geq 30 \text{ Pa} \quad (8)$$

The extrapolated mean wall shear stresses of 130 Pa and 30 Pa for zero mass flux conditions (N = 0 kg/m^2s) represent threshold values below which no mechanical film removal is expected for type A and B films, respectively. Given critical shear stress values, the critical velocities can be easily obtained using Equations (1), (3), and (4). The critical velocities for A and B films

were determined to be $v_{A\ crit}$ = 3.32 m/s (5,279 rpm) and $v_{B\ crit}$ = 3.47 m/s (5,525 rpm), respectively. Interestingly, they turned out to be very close to each other.

Another very important aspect of the turbulent flow around the RC bounded with an outer stationary cylinder (glass cell wall), which distinguishes it from the straight pipe flow, is the presence of pairs of turbulent toroidal counter-rotating vortices whose axes are orientated with the mean flow in a circumferential direction.[28] These vortices, also known as turbulent Taylor vortices (TTV), have previously been visually documented by Andereck et al. and Parker and Merati.[29-30] Apart from the fact that TTV persist up to very large Reynolds numbers (observed at Re = 70,000),[30] it has been found that they cause a nonuniform distribution of the mean wall shear stress, pressure, and turbulent velocity along the cylinder axis.[31] The most severe local effects are concentrated in areas of the vortex outflows from the inner cylinder, which coincide with the maximum mean and fluctuating velocities observed.[31] The numerical simulations carried out by Bilson revealed the existence of secondary pairs of micro-vortices at the vortex outflows, which accounted for the local increase in turbulence levels.[31] Nevertheless, he confirmed that the TV motion had a larger relative contribution to the total momentum and scalar transport than the turbulent part. In addition, a region of negative relative mean pressure was reported in the vicinity of the inner wall, which, according to the author, was indicative of a strong convective effect from the RC.[31] This was particularly true for the vortex outflow locations, where the pressure was significantly lower due to the higher mean velocity.[31]

Mechanical Film Removal Mechanism

Based on the experimental results and limited data available in the open literature on turbulent Taylor-Couette flows, a possible mechanism of mechanical film removal in single-phase flows is proposed. A hypothesis with the sequential steps that take place is as follows:

Separation from the Substrate — The porous sponge-like structure of the iron carbonate film can be seen from a mechanical point of view as a system of springs. The wall shear stress alone is clearly not sufficient to be responsible for film removal. Instead, severe local fluctuating quantities (such as velocity[31] and wall shear stress[19] fluctuations), primarily due to TV motion, impose dynamic mechanical loading (vibrations), which leads to a fatigue-like type of damage. Once the adhesive strength of the film is exceeded, the film starts to separate from the substrate (Figure 19[a]).

Vertical Cracking — Under the influence of the centrifugal forces and/or the negative relative pressure,[31] the gap between the substrate and film tends to increase, and as internal stresses reach the critical value, the vertical cracking occurs (Figure 19[b]).

Crack Opening and Widening — The increased surface roughness at crack locations enhances the local levels of turbulence and promotes further film detachment and lifting from the metal surface (Figure 19[c]).

Film Detachment — The lifted film causes increased drag, at which stage the wall shear stress rips off the protuberant film part. The detached film parts are subsequently blown away from the cylinder by the influence of the centrifugal forces and/or the negative relative pressure (Figure 19[d]).

CONCLUSIONS

❖ The pure mechanical film removal in undisturbed single-phase flow was observed.
❖ When the high velocity/shear is induced, the onset of mechanical film breakdown is delayed due to a crack initiation/growth process. Under the mechanical effect of flow, the film is only partially removed. The film removal kinetics and severity of damage depend on the intensity of the flow, that is, the degree of turbulence.
❖ The mechanism of mechanical film removal has been proposed here by establishing the relationship between the experimental findings and hydrodynamic parameters of interest. It is suspected that the damage of the film is related to the local turbulence levels, which, for a rotating cylinder flow, are a consequence of the Taylor vortex motion. These play a decisive role in the mechanical film removal rather than commonly quoted mean wall shear stress alone.

Further investigations are under way to study film removal by chemical dissolution as well as the possible synergistic effect between the mechanical film removal and dissolution in single phase turbulent flows.

ACKNOWLEDGMENTS

The authors acknowledge M. Bilson, Maunsell Australia Pty. Ltd., whose expertise in Taylor-Couette flows was of valuable help in identifying the relationships between fluid mechanics and erosion-corrosion processes. The financial support by the Australian government in the form of an Australian Postgraduate Award Scholarship is acknowledged.

REFERENCES

1. S. Nešić, K.-L.J. Lee, V. Ruzic, "A Mechanistic Model of Iron Carbonate Film Growth and the Effect on CO_2 Corrosion of Mild Steel," CORROSION/2002, paper no. 02237 (Houston, TX: NACE International, 2002).
2. J.L. Dawson, C.C. Shih, "Corrosion Under Flowing Conditions—An Overview and Model," in Flow Induced Corrosion: Fundamental Studies and Industry Experience, eds. K.J. Kennelly, R.H. Hausler, D.C. Silverman, paper no. 2 (Houston, TX: NACE, 1991).
3. R.W. Revie, ed., Uhlig's Corrosion Handbook, 2nd ed., Electrochemical Society Series (New York, NY: John Wiley and Sons, Inc., 2000), p. 249-272.
4. S. Nešić, J. Postlethwaite, Can. J. Chem. Eng. 69, 3 (1991): p. 698.

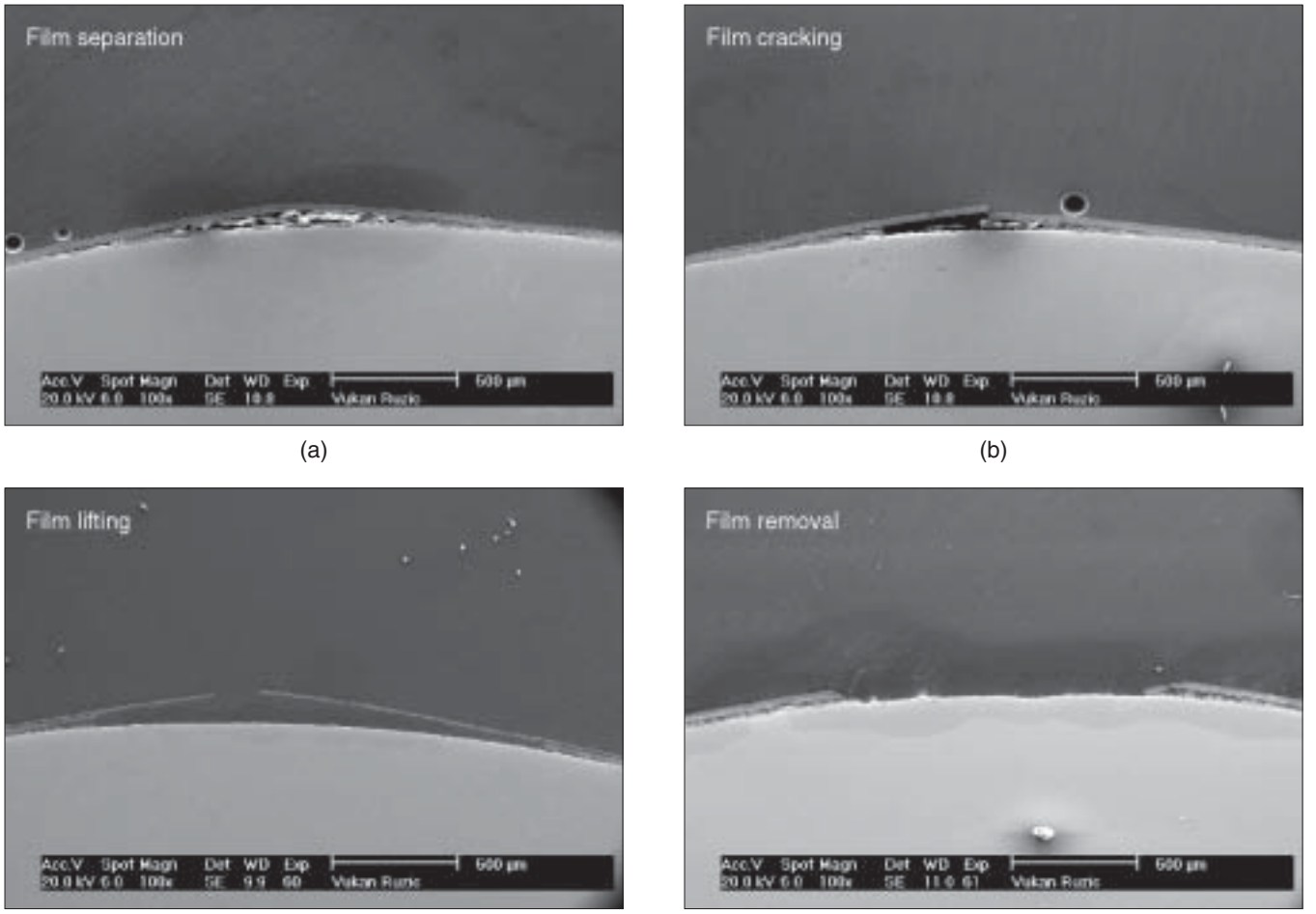

FIGURE 19. *Proposed mechanical film removal mechanism: (a) separation from the substrate, (b) vertical cracking, (c) crack opening and widening, and (d) film detachment.*

5. S. Nešić, J. Postlethwaite, Can. J. Chem. Eng. 69, 3 (1991): p. 704.
6. G. Schmitt, C. Bosch, U. Pankoke, W. Bruckoff, G. Siegmund, "Evaluation of Critical Flow Intensities for FILC in Sour Gas Production," CORROSION/98, paper no. 46 (Houston, TX: NACE, 1998).
7. B.S. Poulson, "Erosion Corrosion," in Corrosion, eds. R.A. Jarman, G.T. Burstein, L.L. Shreir, vol. 2, 3rd ed. (Oxford, U.K.: Butterworth-Heinemann, 1994), p. 1:293.
8. F. Giralt, O. Trass, Can. J. Chem. Eng. 53 (1975): p. 505.
9. F. Giralt, O. Trass, Can. J. Chem. Eng. 54 (1976): p. 148.
10. H. R.Copson, Ind. Eng. Chem. 44 (1952): p. 1,745.
11. B. Craig, Oil Gas J. (1985): p. 99.
12. M.M. Salama, E.S. Venkatesh, "Evaluation of API RP 14E Erosional Velocity Limitations for Offshore Gas Wells," Proc. Offshore Technology Conf., paper no. 4485 (Dallas, TX: Offshore Technology Conference, 1983).
13. B.S. Poulson, Corros. Sci. 35 (1993): p. 655.
14. K.D. Efird, Corrosion 33, 1 (1977): p. 3.
15. D.C. Silverman, Corrosion 40, 5 (1984): p. 220.
16. B.C. Syrett, Corrosion 32, 6 (1976): p. 242.
17. G. Schmitt, T. Gudde, E. Strobel-Effertz, "Fracture Mechanical Properties of CO_2 Corrosion Product Scales and Their Relation to Localized Corrosion," CORROSION/96, paper no. 9 (Houston, TX: NACE, 1996).
18. W. Blatt, E. Heitz, "Hydromechanical Measurements for Erosion-Corrosion," CORROSION/90, paper no. 25 (Houston, TX: NACE, 1990).
19. K.-S. Yang, J.-Y. Hwang, K. Bremhorst, S. Nešić, Can. J. Chem. Eng. 81, 2 (2003): p. 26.
20. V. Ruzic, S. Nešić, "A Study of Iron Carbonate Protective Film Formation," Corrosion and Prevention—2001, paper no. 39 (Newcastle, NSW: Australasian Corrosion Association [ACA], 2001).
21. A. Dugstad, "The Importance of $FeCO_3$ Supersaturation on the CO_2 Corrosion of Carbon Steels," CORROSION/92, paper no. 14 (Houston, TX: NACE, 1992).
22. D.R. Gabe, G.D. Wilcox, J. Gonzales-Garcia, F.C. Walsh, J. Appl. Electrochem. 28 (1998): p. 759.
23. G. Schmitt, M. Mueller, "Critical Wall Shear Stress in CO_2 Corrosion of Carbon Steel," CORROSION/99, paper no. 44 (Houston, TX: NACE, 1999).
24. T. Theodorsen, A. Regier, "Experiments on Drag of Revolving Disks, Cylinders, and Streamline Rods at High Speeds," Natl. Advisory Comm. for Aeronaut. (NACA), Tech. report no. 793, 1944.
25. M. Eisenberg, C.W. Tobias, C.R. Wilke, Chem. Eng. Prog. Symp. Ser. 51, 16 (1954): p. 1.
26. A.C. Makrides, N. Hackerman, J. Electrochem. Soc. 105 (1958): p. 156.
27. R. Kappesser, I. Cornet, R. Grief, J. Electrochem. Soc. 118 (1971): p. 1,957.
28. H. Fasel, O. Booz, J. Fluid Mech. 138 (1984): p. 21.
29. C.D. Andereck, S.S. Liu, H.L. Swinney, J. Fluid Mech. 164 (1986): p. 155.
30. J. Parker, P. Merati, J. Fluids Eng. 118 (1996): p. 810.
31. M.J. Bilson, "Momentum and Scalar Transport in the Straight Pipe and Rotating Cylinder—A Comparison of Transport Mechanisms" (Ph.D. diss., University of Queensland, 2004), p. 247-616.